Distinguishing between hydrogen- and helium-burning red giant stars with asteroseismology

Timothy R. Bedding[1], Benoit Mosser[2], Daniel Huber[1], Josefina Montalbán[3], Paul Beck[4], Jørgen Christensen-Dalsgaard[5], Yvonne P. Elsworth[6], Rafael A. García[7], Andrea Miglio[3], Dennis Stello[1], Timothy R. White[1], Joris De Ridder[4], Saskia Hekker[6,8], Conny Aerts[4,9], Caroline Barban[2], Kevin Belkacem[10], Anne-Marie Broomhall[6], Timothy M. Brown[11], Derek L. Buzasi[12], Fabien Carrier[4], William J. Chaplin[6], Maria Pia Di Mauro[13], Marc-Antoine Dupret[3], Søren Frandsen[5], Ronald L. Gilliland[14], Marie-Jo Goupil[2], Jon M. Jenkins[15], Thomas Kallinger[16], Steven Kawaler[17], Hans Kjeldsen[5], Savita Mathur[18], Arlette Noels[3], Victor Silva Aguirre[19] & Paolo Ventura[20]

[1]*Sydney Institute for Astronomy (SIfA), School of Physics, University of Sydney, NSW 2006, Australia*
[2]*LESIA, CNRS, Université Pierre et Marie Curie, Université Denis Diderot, Observatoire de Paris, 92195 Meudon cedex, France*
[3]*Institut d'Astrophysique et de Géophysique de l'Université de Liège, Allée du 6 Août 17 - B 4000 Liège, Belgium*
[4]*Instituut voor Sterrenkunde, K.U.Leuven, Celestijnenlaan 200D, 3001 Leuven, Belgium*
[5]*Danish AsteroSeismology Centre (DASC), Department of Physics and Astronomy, Aarhus University, DK-8000 Aarhus C, Denmark*
[6]*School of Physics and Astronomy, University of Birmingham, Birmingham B15 2TT, UK*
[7]*Laboratoire AIM, CEA/DSM-CNRS, Université Paris 7 Diderot, IRFU/SAp, Centre de Saclay, 91191, Gif-sur-Yvette, France*
[8]*Astronomical Institute 'Anton Pannekoek', University of Amsterdam, Science Park 904, 1098 XH Amsterdam, The Netherlands*
[9]*IMAPP, Department of Astrophysics, Radboud University Nijmegen, PO Box 9010, 6500 GL Nijmegen, The Netherlands*
[10]*Institut d'Astrophysique Spatiale, UMR 8617, Université Paris XI, Bâtiment 121, 91405 Orsay Cedex, France*
[11]*Las Cumbres Observatory Global Telescope, Goleta, CA 93117, USA*
[12]*Eureka Scientific, 2452 Delmer Street Suite 100, Oakland, CA 94602-3017, USA*
[13]*INAF - IASF, Istituto di Astrofisica Spaziale e Fisica Cosmica, Via del Fosso del Cavaliere 100, 00133 Roma, Italy*
[14]*Space Telescope Science Institute, 3700 San Martin Drive, Baltimore, Maryland 21218, USA*
[15]*SETI Institute/NASA Ames Research Center, MS 244-30, Moffett Field, CA 94035, USA*
[16]*Department of Physics and Astronomy, University of British Columbia, 6224 Agricultural Road, Vancouver, BC V6T 1Z1, Canada*
[17]*Department of Physics and Astronomy, Iowa State University, Ames, IA 50011, USA*
[18]*High Altitude Observatory, NCAR, P.O. Box 3000, Boulder, CO 80307, USA*
[19]*Max-Planck-Institut für Astrophysik, Karl-Schwarzschild-Str. 1, 85748 Garching, Germany*
[20]*INAF - Osservatorio Astronomico di Roma, Via Frascati 33, 00040 Monte Porzio Catone (RM), Italy*

Red giants are evolved stars that have exhausted the supply of hydrogen in their cores and instead burn hydrogen in a surrounding shell[1,2]. Once a red giant is sufficiently evolved, the helium in the core also undergoes fusion[3]. Outstanding issues in our understanding of red giants include uncertainties in the amount of mass lost at the surface prior to helium ignition and the amount of internal mixing from rotation and other processes[4]. Progress is hampered by our inability to distinguish between red giants burning helium in the core and those still only burning hydrogen in a shell. Asteroseismology offers a way forward, being a powerful tool for probing the internal structures of stars using their natural oscillation frequencies[5]. Here we report observations of gravity-mode period spacings in red giants[6] that permit a distinction between evolutionary stages to be made. We use high-precision photometry obtained with the *Kepler* spacecraft over more than a year to measure oscillations in several hundred red giants. We find many stars whose dipole modes show sequences with approximately regular period spacings. These stars fall into two clear groups, allowing us to distinguish unambiguously between hydrogen-shell-burning stars and those that are also burning helium.

Oscillations in red giants, like those in the Sun, are thought to be excited by near-surface convection. The observed oscillation spectra are indeed remarkably solar-like, with a broad range of radial and non-radial modes in a characteristic comb pattern[7–11]. However, theoretical models of red giants[12–16] reveal a more complicated story for the non-radial modes (those with angular degree $l \geq 1$), and it has been suggested that this offers a means for determining the evolutionary states of these stars[15]. Due to the large density gradient outside the helium core, a red giant is effectively divided into two cavities. In the envelope the oscillations have properties of acoustic pressure modes (p modes), but in the core they behave like gravity modes (g modes), with buoyancy as the restoring force. The models predict a very dense spectrum of these so-called mixed modes for each value of l (except $l = 0$, since radial g modes do not exist). Most mixed modes have a much larger amplitude in the core than in the envelope and we refer to them as g-dominated mixed modes. Like pure g modes, they are approximately equally spaced in period[17,18] and measuring their average period spacing (ΔP) would give a valuable new asteroseismic probe of the cores of red giants. Unfortunately, they have very high inertias (the total interior mass that is affected by the oscillation), which leads to a very low amplitude at the stellar surface and makes them essentially impossible to observe. However, because of resonant coupling between the two cavities, some of the mixed modes have an enhanced amplitude in the envelope, making them more like p modes. These p-dominated mixed modes have a lower inertia than the g-dominated mixed modes and so their amplitudes can be high enough to render them observable. We expect their frequencies to be shifted from the regular asymptotic spacing, a feature known as 'mode bumping'[19].

Figure 1a shows theoretical oscillation frequencies in a red giant with a mass of $1.5 M_{\odot}$. The dashed lines show the radial modes ($l = 0$), whose frequencies decrease with time as the envelope of the star expands. These are pure p modes and are approximately equally spaced in frequency, with a separation of $\Delta\nu$. The solid lines show the much denser spectrum of dipole modes ($l = 1$). The g-dominated mixed modes appear as parallel lines whose frequencies increase

with time as the stellar core contracts. These are approximately equally spaced in period. The downward-sloping features that run parallel to the $l = 0$ modes are produced by mode bumping: the p-dominated mixed modes, with frequencies decreasing with age, undergo avoided crossings[19] with the g-dominated mixed modes. A similar pattern of mode bumping and avoided crossings is seen in models of subgiant stars[13,20].

Figure 1b shows the period spacings between adjacent $l = 1$ modes in one of the models, indicated in Fig. 1a with the vertical line. The dips correspond to bumped modes that are squeezed together. The period spacing of the g-dominated modes ($\Delta P_{\rm g}$) can be measured from the upper envelope but cannot be observed directly because only the bumped modes have enough p-mode character to be detected, by virtue of their reduced mode inertias[6,12–14]. Observations will detect only a few modes in each p-mode order, and the average spacings of those observable sequences ($\Delta P_{\rm obs}$) will be less than the true g-mode spacing by up to a factor of two (the actual value depends on the number of modes detected, which is a function of the signal-to-noise in the data, and on the strength of the coupling between the g- and p-mode cavities[20]). Figure 1c shows the mode frequencies of the model in Fig. 1b displayed in échelle format, where the spectrum has been divided into segments that are stacked one above the other. Note that the abscissa shows the period modulo $\Delta P_{\rm g}$, whereas a conventional échelle diagram plots frequencies modulo the p-mode frequency spacing, $\Delta\nu$.

Sequences of $l = 1$ modes with approximately constant period spacings were first observed in the red giant KIC 6928997[6] and we have found similar patterns in several hundred more stars. The observations were obtained with the Kepler satellite over the first 13 months of its mission and were sampled every 29.4 min in the long-cadence mode[21]. Figure 1d shows the period échelle diagram for KIC 6928997 and allows us to estimate the spacing of the g-dominated modes to be $\Delta P_{\rm g} = 77.1$ s, which is the value required to produce a vertical alignment. Remarkably, we have been able to estimate $\Delta P_{\rm g}$ despite the fact that g-dominated modes are not observed (the average spacing of the observed modes[6] is $\Delta P_{\rm obs} \approx 55$ s).

Figure 2 compares observed power spectra of two red giants that have similar p-mode spacings ($\Delta\nu \approx 8\,\mu$Hz) but very different $l = 1$ period spacings. We note that the outermost peaks in each $l = 1$ cluster, which we expect to be the closest in character to the g-dominated modes, appear to be the narrowest. This observation is consistent with theoretical calculations of mode inertias and lifetimes[13–16]. Once again we have detected enough modes to determine $\Delta P_{\rm g}$ unambiguously using échelle diagrams (right panels). We find $\Delta P_{\rm g}$ for the two stars to differ by about a factor of two, implying they have very different core properties.

Inferring $\Delta P_{\rm g}$ in this way using the period échelle diagram is not possible for most of the stars in our sample because it requires at least 3–4 modes to be detected in several of the $l = 1$ clusters, which is only possible for the stars with the best signal-to-noise. Therefore, we have instead measured the average period spacing of the observed $l = 1$ modes ($\Delta P_{\rm obs}$) by using the

power spectrum of the power spectrum. In this method, the power spectrum was first expressed in period rather than frequency and then set to zero in regions not containing power from the $l = 1$ modes, as determined using the methods of ref. 10. The power spectrum of this power spectrum was then calculated in order to determine the most prominent period spacing. For the reasons mentioned above, we expect $\Delta P_{\rm obs}$ to be less than $\Delta P_{\rm g}$ and we have measured this factor to be in the range 1.3–1.6 in the few cases where $\Delta P_{\rm g}$ can be estimated unambiguously. Two other methods to measure $\Delta P_{\rm obs}$ gave comparable results. The first was simply to measure pairwise separations of the strongest $l = 1$ peaks in the power spectrum. The other was to calculate the autocorrelation of the time series[22] with narrow filters centred on the $l = 1$ clusters.

Figure 3a shows observed period spacings for about 400 stars and clearly demonstrates the existence of two distinct populations with different core properties. A comparison with model calculations confirms that the two groups coincide with hydrogen-shell-burning stars on the red giant branch (RGB; blue circles) and those that are also burning helium in the core (red diamonds and orange squares). We conclude that $\Delta P_{\rm obs}$ is an extremely reliable parameter for distinguishing between stars in these two evolutionary stages, which are known to have very different core densities[15] but are otherwise very similar in their fundamental properties (mass, luminosity and radius). Note that other asteroseismic observables, such as the small p-mode separations, are not able to do this[10,15].

Our ability to distinguish between hydrogen- and helium-burning stars makes it possible to investigate their properties as separate populations. One example is the parameter ϵ, which specifies the absolute position of the p-mode comb pattern[10,11]. As shown in Fig. 3b, there is a systematic offset between the two populations. This may indicate a difference in the surface layers, given that ϵ is sensitive to the upper turning point of the modes[23]. However, the difference may also arise because the envelope of oscillation power is centred at different frequencies in the two types of stars (see below). This result is clearly worthy of further study.

A very important application for the helium-burning stars is to distinguish between the so-called red clump and secondary clump[24,25]. The red clump comprises low-mass stars that suffered from electron degeneracy in their hydrogen-shell-burning phase and ignited helium in a flash once the core attained a critical mass. This common core mass explains why the red clump (known as the horizontal branch when seen in metal-poor clusters) spans a very narrow range of luminosities. The secondary-clump stars, meanwhile, are too massive to have undergone a helium flash and so have a range of core masses, and hence of luminosities. The mass threshold that divides these two populations depends on metallicity, and also on core overshoot[24].

Among the helium-burning stars in Fig. 3a we can indeed see this division into a compact group (the clump; red diamonds) and a dispersed group (the secondary clump; orange squares). It is even more apparent when we examine the quantity ${\nu_{\rm max}}^{0.75}/\Delta\nu$, which is approximately independent of luminosity[10] ($\nu_{\rm max}$ is the frequency at which the oscillation envelope has its maximum[26]).

This quantity is shown in Fig. 3c and the comparison with evolutionary models having solar metallicity implies a helium-flash threshold of around $2\,M_{\odot}$. Refinement of this result from more detailed studies of individual stars near the boundary between the clump and secondary clump should test predictions of convective-core overshoot.

1. Schwarzschild, M. & Härm, R. Red Giants of Population II. II. *Astrophys. J.* **136**, 158–165 (1962).

2. Iben, I., Jr. Low-Mass Red Giants. *Astrophys. J.* **154**, 581–595 (1968).

3. Sweigart, A. V. & Gross, P. G. Evolutionary sequences for red giant stars. *Astrophys. J. Suppl. Ser.* **36**, 405–437 (1978).

4. Charbonnel, C. Mixing Along the Red Giant Branch: Where Do We Stand? In T. G. Barnes III & F. N. Bash (ed.) *Cosmic Abundances as Records of Stellar Evolution and Nucleosynthesis*, vol. 336 of *Astronomical Society of the Pacific Conference Series*, 119–130 (2005).

5. Aerts, C., Christensen-Dalsgaard, J. & Kurtz, D. W. *Asteroseismology* (Springer: Heidelberg, 2010).

6. Beck, P. G., Bedding, T. R., Mosser, B. *et al.* Detection of gravity-mode period spacings in red giant stars by the *Kepler* Mission. *Science* (2011). In press.

7. De Ridder, J. *et al.* Non-radial oscillation modes with long lifetimes in giant stars. *Nature* **459**, 398–400 (2009).

8. Kallinger, T. *et al.* Oscillating Red Giants in the CoRoT Exo-field: Asteroseismic Radius and Mass Determination. *Astron. Astrophys.* **509**, A77 (2010).

9. Bedding, T. R. *et al.* Solar-like Oscillations in Low-luminosity Red Giants: First Results from *Kepler*. *Astrophys. J.* **713**, L176–L181 (2010).

10. Huber, D. *et al.* Asteroseismology of Red Giants from the First Four Months of *Kepler* Data: Global Oscillation Parameters for 800 Stars. *Astrophys. J.* **723**, 1607–1617 (2010).

11. Mosser, B. *et al.* The universal red-giant oscillation pattern. An automated determination with CoRoT data. *Astron. Astrophys.* **525**, L9 (2011).

12. Dziembowski, W. A., Gough, D. O., Houdek, G. & Sienkiewicz, R. Oscillations of α UMa and other red giants. *Mon. Not. R. Astron. Soc.* **328**, 601–610 (2001).

13. Christensen-Dalsgaard, J. Physics of solar-like oscillations. *Solar Phys.* **220**, 137–168 (2004).

14. Dupret, M. *et al.* Theoretical amplitudes and lifetimes of non-radial solar-like oscillations in red giants. *Astron. Astrophys.* **506**, 57–67 (2009).

15. Montalbán, J., Miglio, A., Noels, A., Scuflaire, R. & Ventura, P. Seismic Diagnostics of Red Giants: First Comparison with Stellar Models. *Astrophys. J.* **721**, L182–L188 (2010).

16. Di Mauro, M. P. *et al.* Solar-like oscillations from the depths of the red-giant star KIC 4351319 observed with *Kepler*. *Mon. Not. R. Astron. Soc.* (2011). Submitted.

17. Tassoul, M. Asymptotic approximations for stellar nonradial pulsations. *Astrophys. J. Suppl. Ser.* **43**, 469–490 (1980).

18. Miglio, A., Montalbán, J., Eggenberger, P. & Noels, A. Gravity modes and mixed modes as probes of stellar cores in main-sequence stars: From solar-like to β Cep stars. *Astronomische Nachrichten* **329**, 529–534 (2008).

19. Aizenman, M., Smeyers, P. & Weigert, A. Avoided Crossing of Modes of Non-radial Stellar Oscillations. *Astron. Astrophys.* **58**, 41–46 (1977).

20. Deheuvels, S. & Michel, E. New insights on the interior of solar-like pulsators thanks to CoRoT: the case of HD 49385. *Astrophys. Space Sci.* **328**, 259–263 (2010).

21. Jenkins, J. M. *et al.* Initial Characteristics of *Kepler* Long Cadence Data for Detecting Transiting Planets. *Astrophys. J.* **713**, L120–L125 (2010).

22. Mosser, B. & Appourchaux, T. On detecting the large separation in the autocorrelation of stellar oscillation times series. *Astron. Astrophys.* **508**, 877–887 (2009).

23. Gough, D. O. EBK Quantization of Stellar Waves. In Osaki, Y. (ed.) *Hydrodynamic and Magnetodynamic Problems in the Sun and Stars*, 117–143 (Tokyo: Uni. of Tokyo Press, 1986).

24. Girardi, L. A secondary clump of red giant stars: why and where. *Mon. Not. R. Astron. Soc.* **308**, 818–832 (1999).

25. Miglio, A. *et al.* Probing populations of red giants in the galactic disk with CoRoT. *Astron. Astrophys.* **503**, L21–L24 (2009).

26. Kjeldsen, H. & Bedding, T. R. Amplitudes of stellar oscillations: the implications for asteroseismology. *Astron. Astrophys.* **293**, 87–106 (1995).

27. Christensen-Dalsgaard, J. ASTEC – the Aarhus STellar Evolution Code. *Astrophys. Space Sci.* **316**, 13–24 (2008).

28. Kjeldsen, H., Bedding, T. R. & Christensen-Dalsgaard, J. Correcting stellar oscillation frequencies for near-surface effects. *Astrophys. J.* **683**, L175–L178 (2008).

29. Ventura, P., D'Antona, F. & Mazzitelli, I. The ATON 3.1 stellar evolutionary code. A version for asteroseismology. *Astrophys. Space Sci.* **316**, 93–98 (2008).

30. Pietrinferni, A., Cassisi, S., Salaris, M. & Castelli, F. A Large Stellar Evolution Database for Population Synthesis Studies. I. Scaled Solar Models and Isochrones. *Astrophys. J.* **612**, 168–190 (2004).

Supplementary Information is linked to the online version of the paper at www.nature.com/nature, and contains a table listing the data that are shown in Fig. 3.

Acknowledgements We gratefully acknowledge the entire Kepler team, whose outstanding efforts have made these results possible. We thank Michael Biercuk for helpful comments. Funding for this Discovery mission is provided by NASA's Science Mission Directorate. Funding of P.B. and C.A. for this research was received from the European Community's 7th Framework Programme (PROSPERITY). S.H. acknowledges financial support from the Netherlands Organisation for Scientific Research (NWO). The National Center for Atmospheric Research is sponsored by the National Science Foundation.

Author Contributions T.R.B, B.M., P.B., Y.P.E, R.A.G., S.H., C.A., A.-M.B. and F.C. measured and interpreted period spacings; B.M., D.H., R.A.G., S.H., T.K., W.J.C., C.B., D.L.B. and S.M. calculated power spectra and measured large frequency separations; J.M., J.C.-D., A.M., D.S., T.R.W., K.B., M.P.D.M., M.-A.D., M.J.G., S.K., A.N., V.S.A. and P.V. calculated and interpreted theoretical models; J.D.R., S.H., S.F., Y.P.E., D.S., T.M.B., H.K., J.C.-D. and R.L.G contributed to the coordination of the project, including the acquisition and distribution of the data; J.M.J. constructed the photometric time series from the original Kepler pixel data. All authors discussed the results and commented on the manuscript.

Author Information Reprints and permissions information is available at www.nature.com/reprints. The authors declare that they have no competing financial interests. Correspondence and requests for materials should be addressed to T.R.B. (e-mail: t.bedding@physics.usyd.edu.au).

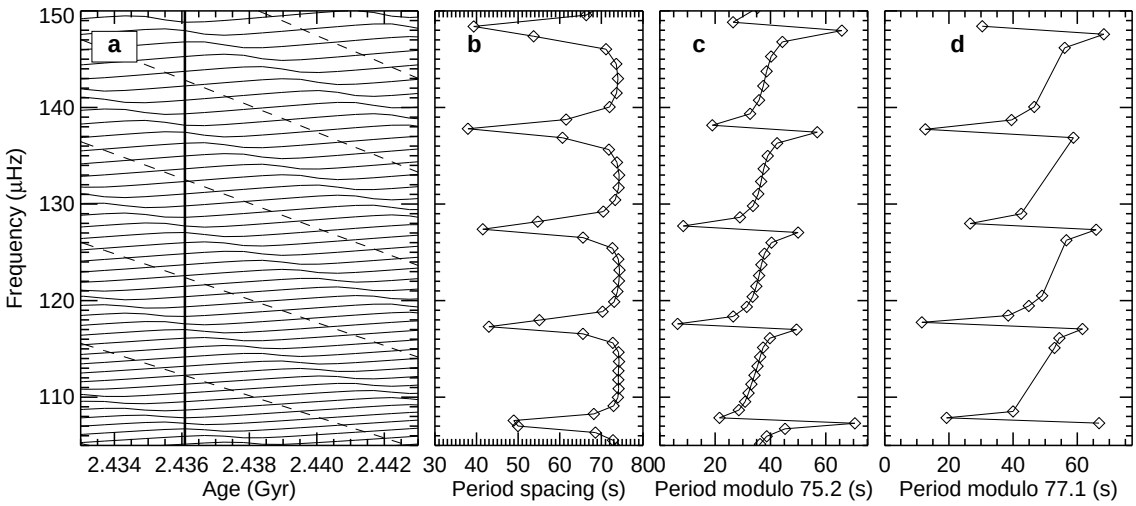

Figure 1 | **Mixed modes and avoided crossings in red giant stars. a**. Evolution with time of oscillation frequencies in a model of a hydrogen-shell-burning red giant with a mass of $1.5 M_\odot$ and solar metallicity, calculated using the Aarhus stellar evolution code ASTEC[27]. Dashed lines show radial modes (with $l = 0$) and solid lines show dipole modes ($l = 1$). The models span ranges in radius and luminosity of 6.3 to 6.7 $R_\odot$ and 19.1 to 21.4 $L_\odot$, respectively. **b**. Period spacings between adjacent $l = 1$ modes for the model marked with a vertical line in panel a. The period spacing of the g-dominated modes ($\Delta P_{\rm g}$) can be seen from the maximum values to be about 75 s. Note that model frequencies were not corrected for near-surface effects[6,28], which would have a small effect on the period spacings. **c**. Échelle diagram of $l = 1$ modes for the same model as shown in panel b. Here, the oscillation spectrum has been divided into segments of fixed length that are stacked one above the other. Note that the abscissa is the period modulo the g-mode period spacing, $\Delta P_{\rm g}$ (whereas a conventional échelle diagram plots frequencies modulo the p-mode frequency spacing, $\Delta\nu$). **d**. Échelle diagram of observed $l = 1$ frequencies in the star KIC 6928997. We conclude that the true g-mode spacing is $\Delta P_{\rm g} = 77.1$ s, whereas the average spacing of the observed modes[6] was found to be $\Delta P_{\rm obs} \approx 55$ s.

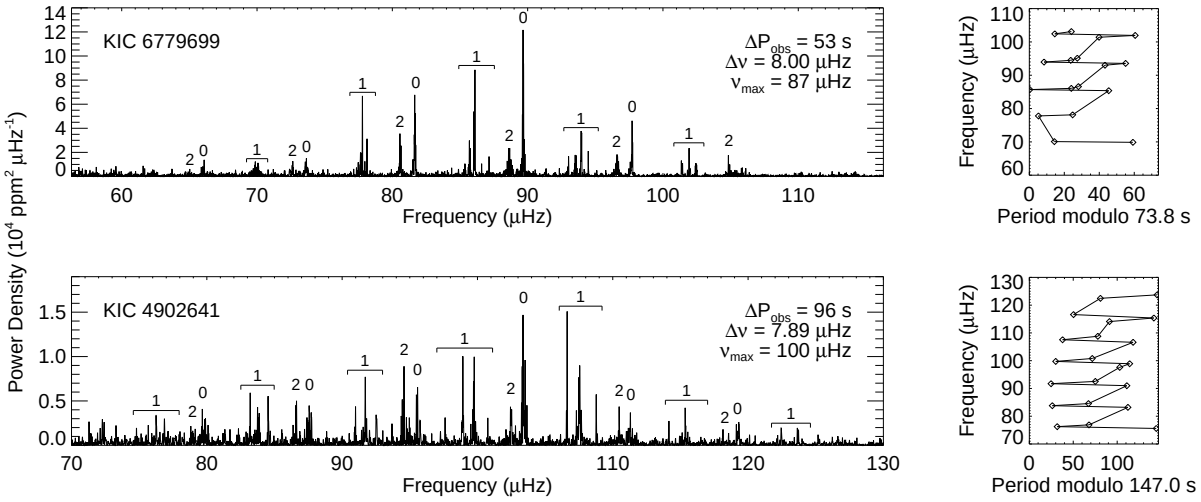

Figure 2 | **Oscillation power spectra and échelle diagrams of two red giant stars observed with Kepler.** The difference in the spacings of the $l = 1$ modes indicates that KIC 6779699 is undergoing hydrogen-shell-burning on the red giant branch, while KIC 4902641 is also burning helium in its core (see Fig. 3). Observations of KIC 6779699 were made over the first 13 months of the Kepler mission (Q0–Q5), while those of KIC 4902641 were made over the first 10 months (Q0–Q4).

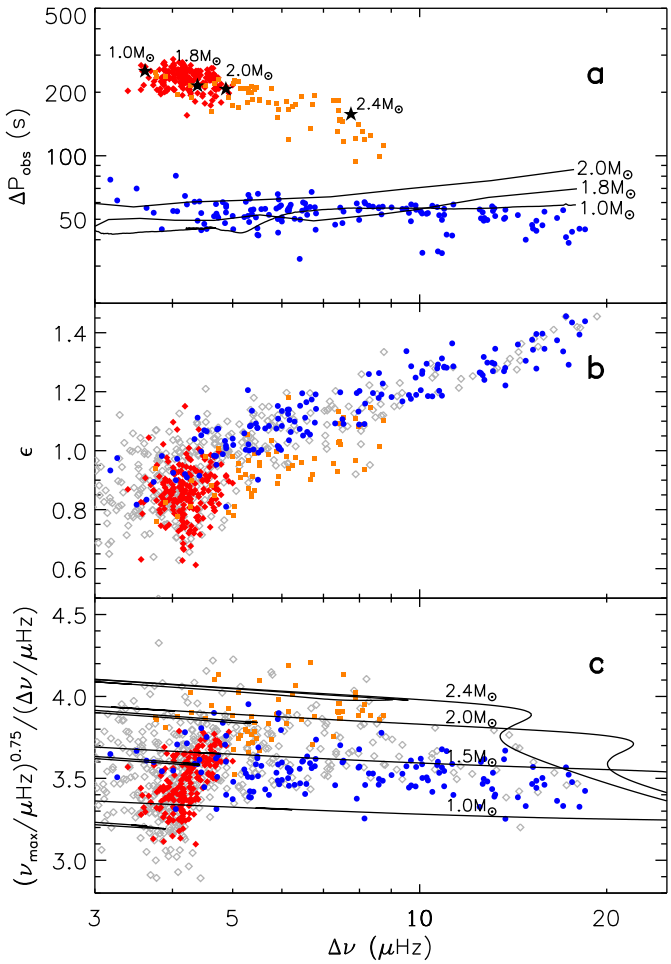

Figure 3 | **Asteroseismic diagrams for red giants observed with Kepler.** The abscissa is the p-mode large frequency separation. **a**. Filled symbols show period spacings measured from observations. The stars divide into two clear groups, with blue circles indicating hydrogen-shell-burning giants (143 stars), while the remainder are helium-core-burning stars (193 red diamonds and 61 orange squares, divided on the basis of panel c). The solid lines show average observable period spacings for ASTEC[27] models of hydrogen-shell-burning giants on the red giant branch as they evolve from right to left, calculated from the central three modes in the $l = 1$ clusters. The black stars show theoretical period spacings calculated in the same way, for four models of helium-core-burning stars that are midway through that phase (core helium fraction 50%). The 2.4-$M_\odot$ model was calculated with ASTEC[27] and commenced helium-burning without passing through a helium flash. The other three models, which did undergo a helium flash, were computed using the ATON code[15,29] (see J. Montalban et al., in prep.). Solar metallicity was adopted for all models, which were computed without mass loss. **b**. The quantity ϵ, which specifies the absolute frequency of the p-mode comb pattern[10,11]. We see a systematic difference between the hydrogen- and helium-burning stars. The open grey diamonds are stars for which a reliable period spacing could not be measured (391 stars). Many of these had high signal-to-noise but lacked a clear structure that would indicate regular period spacings. **c**. The quantity

$\nu_{\rm max}{}^{0.75}/\Delta\nu$, which is approximately independent of luminosity[10]. Helium-burning stars that we identify as belonging to the red clump, based on their positions in this diagram, are marked with red diamonds. The remainder, which presumably belong to the secondary clump, are marked with orange squares. The lines show model calculations based on scaling relations[26] for $\Delta\nu$ and $\nu_{\rm max}$ applied to solar-metallicity BASTI models[30] with the mass loss efficiency parameter set to $\eta = 0.2$.

Supplementary Information

The table lists the red giants that are shown in Figure 3. The columns are: (1) identification number in the Kepler Input Catalogue, (2) large frequency separation, (3) mean observed period spacing of dipole modes, and (4) classification in terms of evolutionary stage. The original Kepler light curves are available via the NASA MAST archive at `http://archive.stsci.edu/`

KIC	$\Delta\nu$ (μHz)	$\Delta P_{\rm obs}$ (s)	Classification
1161618	4.1	—	—
1433593	6.2	—	—
1433730	4.2	—	—
1435573	3.7	—	—
1720425	3.7	—	—
1864183	5.6	56.	RGB
1864855	10.4	—	—
1868101	3.8	234.	red clump
2013502	5.7	—	—
2018392	3.8	—	—
2142095	3.7	—	—
2307683	4.4	—	—
2309469	3.6	—	—
2424822	8.1	—	—
2424934	3.9	—	—
2424955	5.3	—	—
2444348	3.3	—	—
2448225	4.0	228.	red clump
2449703	4.0	248.	red clump
2554924	4.0	205.	red clump
2573092	4.1	—	—
2696732	8.3	58.	RGB
2696955	8.7	—	—
2831788	5.5	45.	RGB
2988638	7.5	149.	secondary clump
2988988	4.3	—	—
3100193	3.5	70.	RGB
3101090	3.9	—	—
3114408	3.4	—	—
3120486	10.6	—	—
3120585	8.5	—	—
3217051	4.3	241.	red clump
3231503	4.3	189.	secondary clump
3323943	4.0	241.	red clump
3339894	3.3	—	—
3355015	3.4	—	—
3425476	4.4	216.	red clump
3426898	6.5	59.	RGB
3443483	10.7	—	—
3444374	5.7	—	—
3455760	4.9	58.	RGB
3457618	3.6	—	—
3526061	10.7	57.	RGB
3529276	5.7	—	—
3530520	4.0	—	—
3530823	4.7	241.	red clump
3531478	17.2	41.	RGB
3560181	3.9	—	—
3631092	14.0	—	—
3631402	4.9	213.	red clump
3642038	4.3	—	—
3656231	4.3	205.	red clump
3660820	4.0	208.	red clump
3729799	4.2	—	—
3730953	5.0	219.	secondary clump
3744043	9.8	58.	RGB
3747777	4.4	—	—
3747860	4.2	—	—
3748585	4.6	—	—
3748691	4.3	245.	red clump
3758458	5.9	166.	secondary clump
3760337	4.3	—	—
3835996	5.0	45.	RGB
3847071	6.1	55.	RGB
3847697	4.9	—	—
3854605	4.3	—	—

KIC	$\Delta\nu$ (μHz)	$\Delta P_{\rm obs}$ (s)	Classification
3858714	4.9	—	—
3860176	6.6	—	—
3867193	4.9	—	—
3869326	4.6	162.	secondary clump
3936921	3.6	268.	red clump
4036007	4.4	241.	red clump
4039306	4.2	268.	red clump
4044238	4.1	241.	red clump
4056266	7.4	149.	secondary clump
4057076	4.6	234.	red clump
4140726	5.0	—	—
4164910	4.5	—	—
4169130	4.3	—	—
4243796	4.3	225.	red clump
4244973	4.7	231.	secondary clump
4249128	4.5	211.	red clump
4249357	5.2	—	—
4262505	8.0	55.	RGB
4269391	4.1	—	—
4271039	5.2	—	—
4275625	3.8	208.	red clump
4276070	4.5	216.	secondary clump
4279700	3.5	—	—
4281702	3.9	238.	red clump
4345370	4.1	—	—
4350501	11.1	42.	RGB
4365609	4.2	268.	red clump
4383388	4.9	54.	RGB
4445711	4.3	248.	red clump
4448777	17.0	55.	RGB
4456739	4.3	228.	red clump
4457200	4.5	196.	red clump
4469602	3.6	—	—
4469886	5.5	183.	secondary clump
4475934	4.4	238.	red clump
4489185	8.6	56.	RGB
4545474	3.9	—	—
4546625	4.1	—	—
4548564	6.0	51.	RGB
4553892	4.6	—	—
4570120	7.4	183.	secondary clump
4571402	4.4	—	—
4575645	4.5	219.	red clump
4578488	5.3	49.	RGB
4633907	3.9	—	—
4638317	3.5	—	—
4640537	4.0	205.	red clump
4644949	6.3	50.	RGB
4645692	4.3	222.	red clump
4659706	3.8	—	—
4662939	5.5	185.	secondary clump
4672904	6.1	—	—
4726049	17.9	—	—
4736611	8.0	50.	RGB
4739728	3.5	—	—
4743924	8.1	131.	secondary clump
4750456	5.9	50.	RGB
4755467	4.4	252.	red clump
4760954	4.8	219.	red clump
4764420	4.4	—	—
4770846	5.5	211.	secondary clump
4773539	4.5	—	—
4813971	4.0	—	—
4818830	4.7	—	—
4828670	4.5	177.	red clump
4843143	3.9	208.	red clump
4845272	3.6	—	—
4857853	3.9	222.	red clump
4902641	7.9	94.	secondary clump
4902701	4.1	—	—
4930906	3.9	—	—
4933594	4.1	248.	red clump
4937204	4.4	49.	RGB
4937576	3.6	—	—
4949422	4.7	219.	secondary clump
4950323	5.9	56.	RGB
4952717	15.5	—	—
4991033	5.3	—	—
4991732	8.5	—	—
5005217	4.4	198.	red clump
5006817	11.7	—	—
5008996	3.7	—	—

KIC	$\Delta\nu$ (μHz)	$\Delta P_{\rm obs}$ (s)	Classification
5016549	8.7	—	—
5017711	4.1	—	—
5023732	3.1	—	—
5023889	5.4	—	—
5024043	5.6	—	—
5024967	4.7	—	—
5026008	6.1	—	—
5032140	4.7	—	—
5034571	5.8	—	—
5084662	4.6	260.	red clump
5087542	3.8	248.	secondary clump
5088362	4.1	196.	secondary clump
5095946	4.3	—	—
5104573	4.0	260.	red clump
5112288	4.8	—	—
5112361	6.2	—	—
5112373	4.7	—	—
5112387	4.7	—	—
5112744	4.4	—	—
5113041	4.0	—	—
5121605	4.1	256.	red clump
5128171	5.4	213.	secondary clump
5172229	4.4	—	—
5196152	7.3	—	—
5199906	5.8	—	—
5266416	3.8	225.	red clump
5269165	3.8	205.	red clump
5270933	4.2	222.	red clump
5283798	5.4	185.	secondary clump
5284127	4.0	234.	red clump
5285357	4.0	—	—
5287610	6.2	57.	RGB
5288607	5.7	179.	secondary clump
5288716	4.3	205.	red clump
5307203	5.3	52.	RGB
5339823	4.3	—	—
5356201	15.9	54.	RGB
5360757	4.2	—	—
5364240	6.8	57.	RGB
5380775	5.9	66.	RGB
5385518	5.3	65.	RGB
5392657	4.6	—	—
5426041	5.1	—	—
5430779	10.5	—	—
5436082	4.4	231.	red clump
5437909	15.3	—	—
5457811	3.6	57.	RGB
5514079	7.8	—	—
5514974	4.0	—	—
5515314	10.9	50.	RGB
5517118	3.9	—	—
5517442	4.0	—	—
5526083	4.6	241.	red clump
5530598	8.7	53.	RGB
5546141	7.5	48.	RGB
5546749	4.0	—	—
5597397	5.1	—	—
5598789	5.4	—	—
5599763	3.8	—	—
5611192	8.0	—	—
5648894	6.2	120.	secondary clump
5694720	3.3	—	—
5700368	4.2	—	—
5709667	8.1	—	—
5770923	7.1	—	—
5782127	3.6	216.	red clump
5787509	3.8	203.	red clump
5790837	4.7	52.	RGB
5791135	4.4	—	—
5791844	5.3	200.	secondary clump
5795250	5.2	—	—
5806522	5.9	43.	RGB
5854149	4.4	—	—
5857618	6.3	—	—
5858034	4.4	—	—
5858947	14.5	—	—
5859492	4.1	—	—
5866737	6.5	55.	RGB
5872509	4.4	—	—
5887977	3.2	77.	RGB
5900096	3.9	216.	red clump
5940228	3.1	—	—

KIC	$\Delta\nu$ (μHz)	$\Delta P_{\rm obs}$ (s)	Classification
5943345	4.7	—	—
5950394	4.2	225.	red clump
5959615	3.6	—	—
5983299	5.9	177.	secondary clump
5990753	7.5	117.	secondary clump
6029189	6.7	57.	RGB
6029474	7.2	—	—
6033938	13.2	52.	RGB
6037660	4.1	—	—
6037858	4.6	—	—
6043187	6.3	—	—
6099979	4.6	—	—
6103934	8.4	—	—
6104786	13.8	—	—
6115575	4.9	—	—
6117517	10.1	53.	RGB
6118479	6.0	58.	RGB
6123202	5.5	42.	RGB
6144777	10.9	56.	RGB
6185790	4.7	—	—
6188269	5.7	—	—
6191288	3.2	—	—
6196149	3.7	216.	red clump
6198581	4.6	248.	red clump
6231193	3.9	—	—
6264398	4.1	—	—
6276948	7.4	147.	secondary clump
6279491	3.8	—	—
6304081	5.9	153.	secondary clump
6357879	4.7	260.	red clump
6363090	4.6	228.	red clump
6371008	3.8	196.	red clump
6424157	8.8	—	—
6448010	4.1	222.	red clump
6451238	3.9	—	—
6465610	4.4	252.	red clump
6500038	5.4	—	—
6508328	4.3	228.	red clump
6508943	4.2	248.	red clump
6547007	4.6	—	—
6579495	8.2	59.	RGB
6579998	4.4	252.	red clump
6586554	5.4	—	—
6593623	4.2	156.	red clump
6606106	4.0	264.	red clump
6610828	4.1	245.	red clump
6612293	4.5	44.	RGB
6665058	9.7	59.	RGB
6690139	9.7	49.	RGB
6696436	3.2	—	—
6755907	4.8	—	—
6762022	4.4	—	—
6768319	5.6	—	—
6779699	8.0	56.	RGB
6780490	4.2	—	—
6804138	7.3	183.	secondary clump
6805631	4.5	—	—
6837256	4.1	—	—
6838420	3.5	—	—
6838707	4.1	248.	red clump
6843557	4.9	—	—
6849167	4.2	—	—
6851499	5.6	56.	RGB
6853465	7.5	—	—
6854095	3.9	—	—
6860004	15.8	—	—
6925158	8.0	—	—
6928997	10.0	54.	RGB
6929729	6.1	—	—
6939158	3.5	—	—
6949816	7.9	59.	RGB
6951925	4.7	205.	red clump
6952430	4.3	245.	red clump
6964342	4.4	—	—
7006979	4.1	—	—
7018252	3.5	—	—
7031016	4.2	219.	red clump
7039075	4.8	211.	red clump
7044886	4.3	216.	secondary clump
7048889	3.8	—	—
7060732	10.9	35.	RGB
7092067	5.5	66.	RGB

KIC	$\Delta\nu$ (μHz)	$\Delta P_{\rm obs}$ (s)	Classification
7093179	3.7	54.	RGB
7103297	4.4	234.	red clump
7109120	6.0	—	—
7118721	6.1	181.	secondary clump
7177015	7.5	—	—
7206531	4.7	208.	red clump
7258771	7.5	57.	RGB
7259653	4.4	61.	RGB
7270142	5.5	51.	RGB
7272257	3.0	—	—
7289277	3.9	—	—
7293609	3.7	—	—
7294715	4.7	238.	red clump
7297940	8.1	—	—
7303187	3.4	—	—
7340724	10.6	—	—
7346365	5.3	—	—
7346442	5.2	51.	RGB
7365701	4.1	277.	red clump
7374855	3.7	—	—
7382407	4.7	51.	RGB
7384523	4.1	213.	red clump
7420223	4.3	—	—
7429055	6.2	56.	RGB
7435143	6.2	59.	RGB
7439931	17.4	39.	RGB
7445698	4.2	64.	RGB
7448051	3.9	—	—
7457184	5.9	62.	RGB
7466616	6.3	175.	secondary clump
7500388	4.7	53.	RGB
7513379	9.1	—	—
7523875	7.7	—	—
7529215	8.3	—	—
7581399	6.7	134.	secondary clump
7581822	13.1	58.	RGB
7584122	18.5	45.	RGB
7587099	3.9	238.	secondary clump
7594865	3.9	219.	red clump
7595285	3.8	—	—
7596701	5.1	—	—
7611069	12.6	54.	RGB
7618122	7.0	—	—
7619034	4.7	—	—
7619745	13.1	55.	RGB
7626457	13.3	—	—
7670419	3.7	—	—
7674224	10.7	35.	RGB
7677317	3.1	—	—
7685724	4.2	260.	red clump
7693833	4.0	80.	RGB
7697146	5.8	208.	secondary clump
7701048	4.2	—	—
7732335	7.7	—	—
7749249	6.7	—	—
7771603	3.8	238.	secondary clump
7808227	4.1	—	—
7820638	4.9	211.	red clump
7821234	4.2	—	—
7831348	4.1	—	—
7868532	7.1	—	—
7888403	5.3	—	—
7905696	4.6	—	—
7919558	4.0	—	—
7935931	3.9	—	—
7944142	7.0	—	—
7948086	4.5	234.	red clump
7949599	4.2	241.	red clump
7955392	4.2	—	—
7957166	14.3	—	—
8005116	4.3	—	—
8039416	4.0	231.	red clump
8045883	4.0	234.	red clump
8056874	5.3	208.	secondary clump
8078554	4.3	256.	red clump
8081278	3.8	—	—
8081535	4.6	228.	red clump
8086192	7.1	—	—
8087067	9.0	57.	RGB
8094602	5.5	—	—
8099073	4.4	252.	red clump
8120076	4.0	—	—

KIC	$\Delta\nu$ (μHz)	$\Delta P_{\rm obs}$ (s)	Classification
8123843	3.7	—	—
8144529	4.4	—	—
8154383	6.4	32.	RGB
8160590	4.1	—	—
8173148	4.2	222.	red clump
8173725	5.0	228.	secondary clump
8195595	6.5	60.	RGB
8196436	4.2	—	—
8210100	4.5	191.	red clump
8232851	4.8	—	—
8233917	3.8	—	—
8235013	3.7	252.	red clump
8246635	4.5	216.	red clump
8248948	3.4	—	—
8278906	4.0	—	—
8284032	4.3	—	—
8293158	4.2	234.	red clump
8307630	3.9	273.	red clump
8310792	8.3	—	—
8343654	3.3	—	—
8350645	5.3	—	—
8359169	5.3	—	—
8366239	13.7	51.	RGB
8377116	3.9	—	—
8378462	7.4	131.	secondary clump
8378653	7.4	163.	secondary clump
8386921	3.5	—	—
8396782	7.1	—	—
8397081	5.9	—	—
8410006	3.9	—	—
8410637	4.6	—	—
8415501	3.6	—	—
8431695	6.1	56.	RGB
8432239	4.9	—	—
8458519	3.9	252.	red clump
8461449	5.2	208.	secondary clump
8462934	6.2	172.	secondary clump
8475025	9.5	56.	RGB
8480097	15.4	44.	RGB
8482522	3.9	219.	red clump
8507397	4.2	248.	red clump
8508931	5.1	—	—
8518198	11.6	—	—
8522040	4.7	—	—
8525359	5.6	—	—
8526108	4.5	245.	red clump
8539201	3.9	252.	red clump
8540615	4.8	208.	red clump
8545504	9.3	—	—
8547390	4.7	225.	red clump
8561238	5.4	200.	secondary clump
8583586	4.4	—	—
8611833	4.2	252.	red clump
8612520	4.2	—	—
8612811	4.1	260.	red clump
8628585	4.2	193.	red clump
8649099	4.5	—	—
8669282	4.4	—	—
8686058	4.7	234.	red clump
8686389	3.0	—	—
8690009	3.7	—	—
8707667	3.9	203.	red clump
8708654	5.4	—	—
8718745	11.3	59.	RGB
8746834	5.9	—	—
8747415	11.3	—	—
8748278	4.0	225.	red clump
8753234	5.4	205.	secondary clump
8757215	4.3	268.	red clump
8771414	4.2	211.	red clump
8803432	4.1	—	—
8812397	6.7	67.	RGB
8813946	6.5	192.	secondary clump
8827934	5.3	—	—
8839028	3.6	—	—
8843610	4.4	252.	red clump
8846187	4.9	198.	red clump
8873797	3.9	256.	red clump
8907943	4.0	—	—
8909673	4.7	—	—
8911558	4.5	—	—
8941202	4.1	252.	red clump

KIC	$\Delta\nu$ (μHz)	$\Delta P_{\rm obs}$ (s)	Classification
8955683	4.8	179.	red clump
8962844	4.5	256.	red clump
9002344	4.4	—	—
9009805	5.2	61.	RGB
9027245	5.4	53.	RGB
9028697	6.0	—	—
9072262	4.5	48.	RGB
9075872	13.2	56.	RGB
9086505	4.1	256.	red clump
9088119	4.0	—	—
9112472	4.8	—	—
9115334	6.1	—	—
9115334	6.1	—	—
9139859	6.8	45.	RGB
9145781	17.6	44.	RGB
9145955	10.9	52.	RGB
9150223	4.4	241.	red clump
9157260	18.1	45.	RGB
9159227	3.8	256.	red clump
9173371	8.0	141.	secondary clump
9176207	5.4	208.	secondary clump
9210413	19.3	—	—
9240941	8.3	—	—
9265513	5.3	55.	RGB
9267654	10.3	53.	RGB
9268146	3.6	—	—
9269772	5.9	—	—
9300159	12.7	51.	RGB
9307073	4.8	—	—
9327993	4.1	—	—
9328135	5.8	—	—
9329200	6.8	53.	RGB
9332840	4.5	222.	red clump
9333501	3.5	—	—
9340114	3.5	—	—
9346288	3.4	—	—
9349632	7.9	121.	secondary clump
9351617	4.4	—	—
9390293	3.8	234.	red clump
9392039	4.1	—	—
9396363	4.6	198.	red clump
9427247	8.8	112.	secondary clump
9427889	3.7	—	—
9430402	6.2	166.	secondary clump
9430786	4.1	—	—
9447310	7.3	47.	RGB
9456598	4.5	—	—
9475697	9.9	55.	RGB
9511938	4.9	—	—
9542218	5.8	—	—
9551036	5.7	52.	RGB
9569462	3.5	—	—
9574650	9.6	54.	RGB
9579860	5.9	57.	RGB
9583430	7.9	—	—
9589500	8.3	124.	secondary clump
9589638	4.4	—	—
9611634	3.4	203.	red clump
9631782	6.6	—	—
9635388	4.4	238.	red clump
9635649	15.2	45.	RGB
9640886	4.0	55.	RGB
9641772	4.2	222.	red clump
9650046	6.1	—	—
9650527	5.3	179.	secondary clump
9652494	4.6	—	—
9658002	4.1	—	—
9705636	4.0	—	—
9705687	6.7	175.	secondary clump
9706194	3.3	—	—
9711231	5.1	—	—
9711492	5.1	225.	secondary clump
9711510	5.1	208.	secondary clump
9716866	3.8	—	—
9728845	3.1	—	—
9761597	5.8	—	—
9767815	8.2	60.	RGB
9777536	4.7	—	—
9778288	5.2	—	—
9780183	3.8	—	—
9791929	4.5	—	—
9818513	3.9	231.	red clump

KIC	$\Delta\nu$ (μHz)	$\Delta P_{\rm obs}$ (s)	Classification
9818604	3.5	—	—
9835436	3.1	—	—
9835626	5.4	—	—
9882316	13.7	50.	RGB
9882550	4.2	205.	red clump
9884818	4.3	234.	red clump
9896174	18.1	—	—
9902962	6.8	193.	secondary clump
9933754	4.2	245.	red clump
9967351	5.7	—	—
9968040	5.0	52.	RGB
9992544	3.4	—	—
10006158	4.0	—	—
10010946	4.7	52.	RGB
10011329	3.8	—	—
10016093	3.8	—	—
10055196	8.8	—	—
10062594	4.8	—	—
10068810	5.4	56.	RGB
10070717	4.1	—	—
10080974	4.6	238.	red clump
10090400	3.9	252.	red clump
10095409	4.2	59.	RGB
10118422	4.7	231.	red clump
10118929	4.3	—	—
10122158	14.4	—	—
10123207	13.7	55.	RGB
10124436	4.9	—	—
10136291	4.1	—	—
10145279	3.6	—	—
10161943	6.3	—	—
10186053	4.0	248.	red clump
10186608	4.2	225.	red clump
10188141	4.3	—	—
10188964	4.4	241.	red clump
10190733	3.8	—	—
10192458	10.5	58.	RGB
10196240	4.1	—	—
10200377	12.5	56.	RGB
10202184	12.7	49.	RGB
10207321	6.7	—	—
10213931	4.5	45.	RGB
10220213	16.4	—	—
10221370	4.5	222.	red clump
10252281	4.2	273.	red clump
10257278	12.2	—	—
10257419	8.4	57.	RGB
10257683	3.8	—	—
10286616	4.2	277.	red clump
10290315	4.2	234.	red clump
10297313	8.2	119.	secondary clump
10323222	4.9	48.	RGB
10328946	4.1	—	—
10332186	3.2	—	—
10351792	3.6	—	—
10353044	4.2	273.	red clump
10383668	4.9	189.	secondary clump
10386904	14.8	40.	RGB
10388249	5.4	—	—
10389037	4.1	—	—
10389393	4.5	54.	RGB
10403323	3.7	234.	red clump
10404994	4.5	216.	red clump
10426854	4.4	—	—
10456555	4.8	—	—
10467570	4.0	264.	red clump
10474071	7.5	145.	secondary clump
10483504	8.7	—	—
10489073	4.1	219.	red clump
10527754	6.0	49.	RGB
10533369	4.3	—	—
10552202	4.3	61.	RGB
10592249	4.2	—	—
10593078	15.4	49.	RGB
10602374	4.3	211.	red clump
10619191	4.4	—	—
10651578	4.2	—	—
10659688	3.2	—	—
10662618	4.0	231.	red clump
10709799	4.2	—	—
10711145	4.2	208.	red clump
10711154	4.7	—	—

KIC	$\Delta\nu$ (μHz)	$\Delta P_{\rm obs}$ (s)	Classification
10716853	5.0	216.	red clump
10721900	4.2	231.	red clump
10724027	4.0	—	—
10743515	4.5	—	—
10747240	4.1	252.	red clump
10749112	5.2	—	—
10776256	13.2	—	—
10777816	15.8	47.	RGB
10778969	4.3	193.	red clump
10779177	17.2	—	—
10796378	4.7	—	—
10799530	4.3	225.	red clump
10816748	3.8	45.	RGB
10842231	4.3	200.	red clump
10847321	6.6	52.	RGB
10858520	3.8	—	—
10859779	7.3	—	—
10864711	4.9	—	—
10866415	8.7	57.	RGB
10903016	3.3	—	—
10907196	4.7	191.	red clump
10910889	4.7	208.	red clump
10918731	4.7	191.	red clump
10922821	3.5	—	—
10961390	4.0	—	—
10965536	3.3	61.	RGB
10973854	3.6	—	—
10977629	3.2	—	—
11018922	4.2	264.	red clump
11028372	4.6	—	—
11028575	4.3	—	—
11043208	5.4	—	—
11043832	5.7	—	—
11046496	3.9	—	—
11083701	3.9	200.	red clump
11084022	4.7	59.	RGB
11126721	3.8	—	—
11128910	4.2	256.	red clump
11129153	3.7	—	—
11138375	4.0	248.	red clump
11153989	4.1	—	—
11177727	3.8	—	—
11177749	4.1	—	—
11188067	4.2	222.	red clump
11190322	5.5	42.	RGB
11199105	3.8	—	—
11228759	4.1	55.	RGB
11231549	3.5	—	—
11236536	4.6	—	—
11247049	3.9	268.	red clump
11250152	3.6	—	—
11251115	5.1	170.	secondary clump
11252233	3.7	225.	red clump
11282383	7.2	—	—
11296211	4.0	—	—
11308784	6.2	55.	RGB
11339000	4.3	256.	red clump
11340165	4.0	287.	red clump
11342694	7.1	—	—
11353313	10.8	52.	RGB
11359175	4.2	234.	red clump
11403437	4.2	248.	red clump
11409529	4.2	231.	red clump
11410549	4.2	—	—
11456449	9.4	—	—
11465784	4.3	252.	red clump
11509277	4.7	245.	red clump
11518492	5.4	—	—
11521352	9.2	—	—
11550492	8.6	57.	RGB
11550567	4.1	252.	red clump
11551628	5.0	173.	secondary clump
11551746	4.7	213.	red clump
11564787	3.6	252.	red clump
11568605	4.9	—	—
11569659	4.1	245.	red clump
11612171	4.0	268.	red clump
11617501	4.8	—	—
11617622	3.9	208.	red clump
11618103	9.4	56.	RGB
11657684	4.1	222.	red clump
11658270	3.1	—	—

KIC	$\Delta\nu$ (μHz)	$\Delta P_{\rm obs}$ (s)	Classification
11668246	4.3	—	—
11673900	4.6	173.	red clump
11674666	4.0	273.	red clump
11674677	3.9	277.	red clump
11704163	4.8	—	—
11707304	4.2	219.	red clump
11707798	4.3	228.	red clump
11721438	8.6	99.	secondary clump
11752358	6.6	56.	RGB
11753722	5.3	—	—
11754056	4.2	241.	red clump
11757739	4.4	248.	red clump
11758710	5.2	—	—
11805460	4.3	213.	red clump
11805792	4.1	225.	red clump
11817405	3.8	—	—
11821439	4.8	60.	RGB
11860626	4.9	57.	RGB
11861823	3.0	—	—
11868246	3.8	—	—
11905840	10.3	54.	RGB
11913545	10.1	35.	RGB
11961545	5.3	63.	RGB
11968334	11.3	42.	RGB
11973853	14.6	—	—
12007304	16.6	51.	RGB
12008797	4.0	—	—
12008916	12.8	50.	RGB
12012082	3.3	—	—
12012725	3.3	—	—
12021906	4.6	231.	red clump
12058556	9.3	—	—
12061622	4.2	225.	red clump
12070114	4.3	—	—
12104584	3.6	205.	red clump
12109388	4.3	181.	red clump
12110266	4.3	198.	red clump
12116393	6.3	—	—
12121207	3.6	264.	red clump
12152850	4.0	252.	red clump
12159715	6.4	50.	RGB
12168406	4.7	—	—
12169845	3.3	—	—
12203243	15.2	47.	RGB
12208273	3.0	—	—
12217239	3.2	—	—
12302516	4.1	234.	red clump
12306695	3.8	—	—
12316494	3.8	—	—
12366461	4.6	—	—
12454201	4.3	245.	red clump
12455504	3.9	—	—
12458003	3.8	—	—
12470054	12.6	51.	RGB
12507577	7.5	54.	RGB
12519768	3.2	—	—
12520106	4.4	245.	red clump
12555902	4.1	—	—
12599612	5.4	—	—
12599878	4.1	256.	red clump
12601771	14.4	52.	RGB
12603035	3.9	238.	red clump
12688781	4.6	183.	red clump